In situ steel solidification imaging in continuous casting using magnetic induction tomography

OPEN ACCESS
IOP Publishing
Measurement Science and Technology
Meas. Sci. Technol. **31** (2020) 065401 (14pp)
https://doi.org/10.1088/1361-6501/ab6f30

In situ steel solidification imaging in continuous casting using magnetic induction tomography

Manuchehr Soleimani[1], Fang Li[1], Stefano Spagnul[2], Juan Palacios[3], José I Barbero[3], Teresa Gutiérrez[3] and Alberto Viotto[4]

[1] Engineering Tomography Lab (ETL), Department of Electronic and Electrical Engineering, University of Bath, Bath, United Kingdom
[2] Product Division, Ergolines Lab s.r.l., Area Science Park, Bldg. R3 Padriciano, Trieste 34149, Italy
[3] Tecnalia, Parque Científico y Tecnológico de Bizkaia, Astondo Bidea, Edificio 700, E-48160 Derio, Bizkaia, Spain
[4] Ferriere Nord, Via delle Ferriere, 33010 Zona Industriale di Rivoli di Osoppo UD, Italy

E-mail: m.soleimani@bath.ac.uk

Received 25 November 2019, revised 15 January 2020
Accepted for publication 23 January 2020
Published 12 March 2020

Abstract

The solidification process in continuous casting is a critical part of steel production. The speed and quality of the solidification process determines the quality of the final product. Computational fluid dynamics (CFD) simulations are often used to describe the process and to design its control system but, so far, there has been no tool that provides an online measurement of the solidification front of hot steel during the continuous casting process. This paper presents a novel magnetic induction tomography (MIT) solution, developed in the EU-funded SHELL-THICK project, to work in a real casting setting and to provide a real-time and reliable measurement of the shell thickness in a cross section of the strand. The new MIT system was installed at the end of the secondary cooling chamber of a casting unit and tested over several days in a real production process. MIT is able to create an internal map of the electrical conductivity of hot steel deep inside the billet. The image of electrical conductivity is then converted to a temperature profile that allows the measurement of the solid, mushy and liquid layers. In this study, such a conversion is done by synchronizing in one time step the MIT measurement and the thermal map generated with the actual process parameters available at that time. The MIT results were then compared with the results obtained with the CFD and thermal modelling of the industrial process. This is the first time *in situ* monitoring of the interior structure has been carried out during a real continuous casting.

Keywords: steel solidification, shell thickness, continuous casting process, CFD modelling, magnetic induction tomography

(Some figures may appear in colour only in the online journal)

1. Introduction

The dynamic of the steel solidification processes in continuous casting has been the subject of many scientific studies [1, 2]. Theoretical models are proposed to partially describe the parameters that affect these processes, such as thermal convection either in a different metal such as aluminium or in lab-based tests [3–5]. Laboratory experiments are possible using x-ray computed tomography to demonstrate different phases of structures [6, 7]. Real-time monitoring of the process was not possible due to the harsh environment of the real casting process. Thermal imaging of the exterior of the casting

billet is possible, but no information from internal structures is available [8, 9].

This paper presents a novel magnetic induction tomography (MIT) solution to work in a real continuous casting machine and to provide a real-time measurement of the shell thickness in a cross section of the strand at the end of the secondary cooling chamber. A laboratory version of the new MIT device was verified in a test with a low melting alloy, demonstrating the potential use of the MIT system for imaging deep inside metallic materials [10]. In these lab-based tests the temperature profile reconstructed in the MIT images were verified with thermocouple data. This paper describes an improved version of the MIT system used in [10], and the results were obtained in the field test for the new tomography device when it was installed in the continuous casting machine of the steel company Ferriere Nord (FENO).

2. The new MIT system

MIT is an emerging and noninvasive imaging technique based on the principle of eddy current induction in conductive media. Induction tomography provides a contactless method of imaging the electrical conductivity of an object: an array of excitation and receiving coils provides multiple measurements of mutual inductances that are used by the tomographic image reconstruction software to image the electrical conductivity distribution [11].

The MIT scenario proposed in the SHELL-THICK project, in order to image the billet inside and visualize the shell thickness of a cross section, is described in figure 1. A probe equipped with a series of coils, which can be alternatively operated in transmission or reception mode, is installed around the billet to create a 2D electrical conductivity map of the billet cross section. Based on the electrical conductivity difference between the solid shell, the mushy region and the liquid core, boundaries between the different domains could be identified.

2.1. The new tomography device

The new MIT device consists of 16 rectangular coils fixed to a square structure surrounding the solidifying billet, each side of the square featuring four coils. Table 1 shows information about the coil design for the MIT system in which an excitation frequency of 130 Hz was used.

The device for the industrial process was developed by following an iterative process. The phase differences between transmitted and received signals are used as MIT data and we collected 240 measurements from 16 sensors ($16 \times 16 - 16$), which gives 120 independent measurements.

First, a dummy prototype was built with a wood structure and tested at FENO facilities to assess the effectiveness of the cooling strategy and the dimensional stability of the system under significant heat radiation. Then, based on the experience acquired during the first test, the tomography device to be installed in the secondary cooling chamber of the continuous casting machine was developed (see figures 2(a) and (b)), replacing the wood structure by a robust stainless steel backbone and introducing a ceramic material, in place of the wood sheets, to avoid any mechanical deformation. The device has a dedicated cooling station to maintain steady state conditions. The cold side of the heat exchanger is connected to the primary circuit of the continuous casting machine. The system includes a refilling tank to compensate leakage of the circuit. Real-time software on a dedicated PC controls the tomographic device and the cooling water station.

The MIT device was installed at the end of the secondary cooling chamber of one of the strands of the continuous casting machine of FENO (figure 2(b)) and was measured over one week. The installation proved to be effective.

Figure 3(b) shows the evolution of the global phase index, that represents the variability of the measurement of the device, and the temperature of the coils, during a whole 24 h casting sequence. The norm of the differences between free space phase data (for all 240 MIT data) and phase data when the billet was present inside the MIT sensor is referred to as theglobal phase index. This is a useful indicator showing how all MIT measurement data are changing. The recorded measure values are quite stable. This shows that there was no major thermal drift and the device was under optimal thermal conditions. This was a test to show that the designed cooling system is suitable for working in the harsh operating conditions.

The MIT system used here was initially calibrated for a similar task in a low temperature solidification test [10]. In [10] we studied the solidification using the MIT system and compared it with the real-time temperature readings from thermocouples inserted inside the liquid wood metal. Such a thermocouple could not have been used in a real casting plant test, but the experiments in [10] show consistency between temperature data and solidification and MIT conductivity mapping.

2.2. Tomographic image reconstruction algorithms

MIT utilizes an array of inductive coils, distributed equally around an imaging region, to visualize the electromagnetic property distribution of the electrical conductivity of an imaging subject. The imaging principle is based on the laws of induction and eddy currents which are induced in an AC magnetic field. The formulation can be obtained from Maxwell's equations [11, 12]:

$$\nabla \times \frac{1}{\mu} \nabla \times A + j\omega\sigma A = J_s \tag{1}$$

where ω is the angular frequency, μ is the permeability, A is the total magnetic vector potential as a result of the effect of eddy current induced by the electrical conductivity σ and the current source J_s.

Equation (1) can be solved by approximating the system as a combination of linear equations in small elements with appropriate boundary conditions using Galerkin's approximation [13]:

$$\int_{\Omega_c+\Omega_s} \left(\nabla \times N_i \cdot \frac{1}{\mu} \nabla \times A \right) \mathrm{d}v + \int_{\Omega_c+\Omega_s} (j\omega\sigma N_i \cdot A)\, \mathrm{d}v = \int_{\Omega_s} (\nabla \times N_i \cdot T_s)\, \mathrm{d}v \tag{2}$$

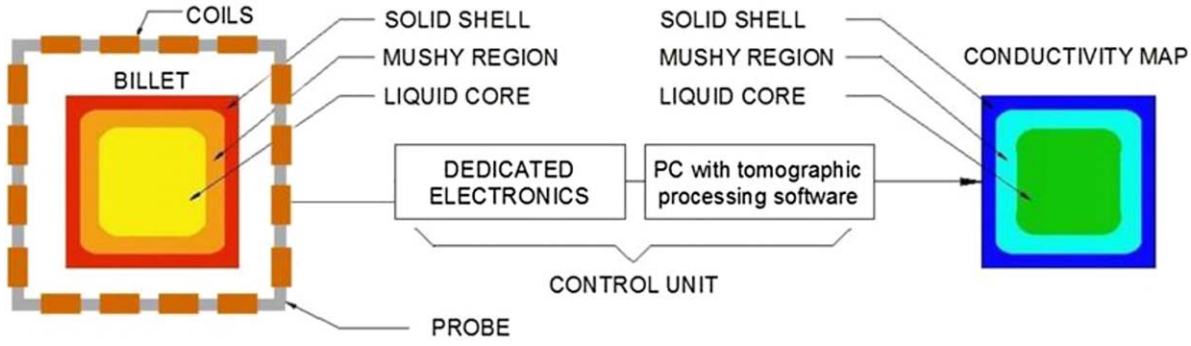

Figure 1. MIT system scenario proposed in the SHELL-THICK project to obtain the shell thickness in a cross section of the billet.

Table 1. Real geometry of the model.

Billet size	160 × 160 mm
Coil internal diameter	50 mm
Coil external diameter	65 mm
Coil height	10 mm
Coil thickness	7.5 mm
No. turns	825

where T_s is the electric vector potential and $J_s = \nabla \times T_s$, N_i is the linear combination of edge shape functions, and Ω_C and Ω_S are eddy current region and current source region or excitation coil region, respectively.

The right hand side of equation (2) can be solved with the aid of Biot–Savart's law. When J_0 is the unit current density passing through the coil, the measured induced voltage in the sensing coil can be calculated:

$$V_{mn} = -j\omega \int_{\Omega_s} (A \cdot J_0)\, \mathrm{d}v. \tag{3}$$

Then the Jacobian matrix can be formulated by

$$J = \frac{\partial V_{mn}}{\partial \sigma_x} = -\omega^2 \frac{\int_{\Omega_x} A_m \cdot A_n \mathrm{d}v}{I} \tag{4}$$

where σ_x is the conductivity of pixel x and Ω_x is the volume of the perturbation, A_n is the forward solver of the sensor coil excited by the unit current, A_m is the forward solver of excitation coil m excited with I. Several laboratory-based experiments with known shapes and materials were used to compare the output of the forward model, the phase of the inducted voltage from equation (3) and real experimental data [10]. This shows that the forward model and lab-based experiments are almost identical. This points to the accuracy of the model as well as the high level of accuracy in the design of the sensor and the electronics. This paper then uses the same instrument and the forward model in the harsh environment of real continuous casting.

The inverse problem in MIT is defined as the retrieval of the unknown electrical conductivity distributions of the target from the measured voltage V_{measured} [14]:

$$V_{\text{measured}} - F(\sigma_0) = J(\sigma - \sigma_0) \tag{5}$$

where σ_0 is the initial estimate conductivity, $F(\sigma_0)$ is the initial estimate voltage obtained from forward problem, J is the Jacobian matrix obtained from the forward problem.

Ordinarily, the inverse problem can be characterized by solving the least-square problem:

$$\sigma_\alpha = argmin_{\Delta\sigma}(\|J\Delta\sigma - \Delta v\|^2). \tag{6}$$

A state-of-the-art total variation regularization, defined by adding a penalty term to equation (6), has been carried out in this paper for solving the inverse problem:

$$\sigma_\alpha = argmin_{\Delta\sigma}(\|J\Delta\sigma - \Delta v\|^2 + \alpha\|\nabla\Delta\sigma\|_1) \tag{7}$$

where α is the regularization parameter, $\|\nabla\Delta\sigma\|_1$ is the total variation functional, ∇ is the gradient and $\|\cdot\|_1$ is the l_1 norm.

The theory of different types of TV inverse solvers has been explained and investigated in detail in [14, 15]. The TV algorithm is to solve the constrained optimization problem:

$$\Delta\sigma = argmin_{\Delta\sigma}\|\nabla\Delta\sigma\|_1 \text{such that } \|J\Delta\sigma - \Delta v\|^2 < \rho \tag{8}$$

where ρ accounts for the noise data.

As anisotropic TV can produce reconstructed images with different properties in every direction. This version of the discrete TV functional is adopted as the proposed algorithm in this paper:

$$\|\nabla\Delta\sigma\|_1 = \alpha_x \|\nabla_x\Delta\sigma\|_1 + \alpha_y \|\nabla_y\Delta\sigma\|_1 + \alpha_z\|\nabla_z\Delta\sigma\|_1. \tag{9}$$

3. Modelling of the continuous casting process

The FENO industrial continuous casting (CC) process was simulated in order to obtain information on billet shell thicknesses for the analysis and validation of the measurements of the new MIT device. The information provided by this simulation about the temperature and thickness evolution along the strand was also very useful for the design and the definition of the location of the MIT device sensors.

Initially, several CFD (computational fluid dynamics) simulations using ANSYS Fluent were performed for the target steel grade of the study (the Fe50 steel grade) and at different casting speeds. But the casting speed during the actual CC process in FENO is not stationary and, in addition, during the MIT

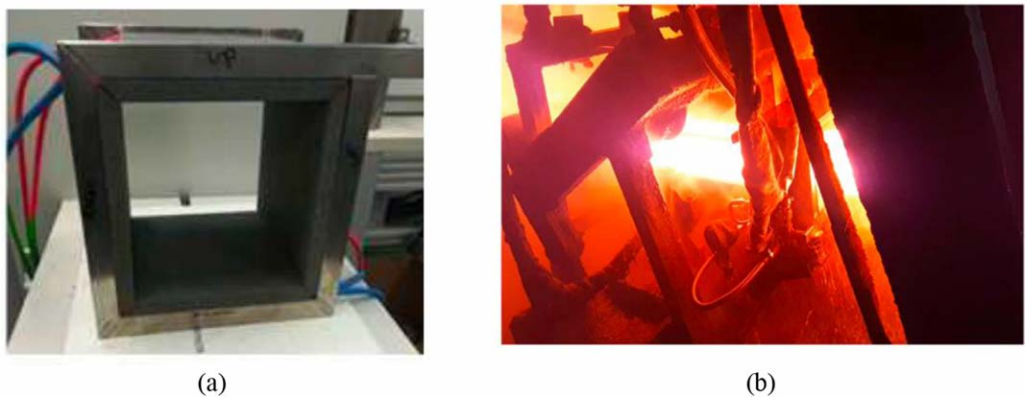

(a) (b)

Figure 2. (a) The MIT device, (b) installation at the end of the secondary cooling chamber of FENO.

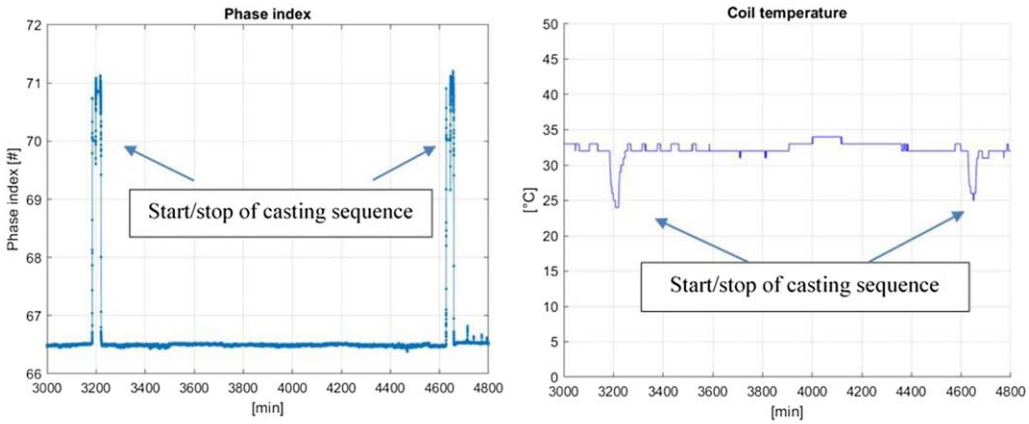

(a) (b)

Figure 3. (a) Global phase index. (b) Coil temperature during casting.

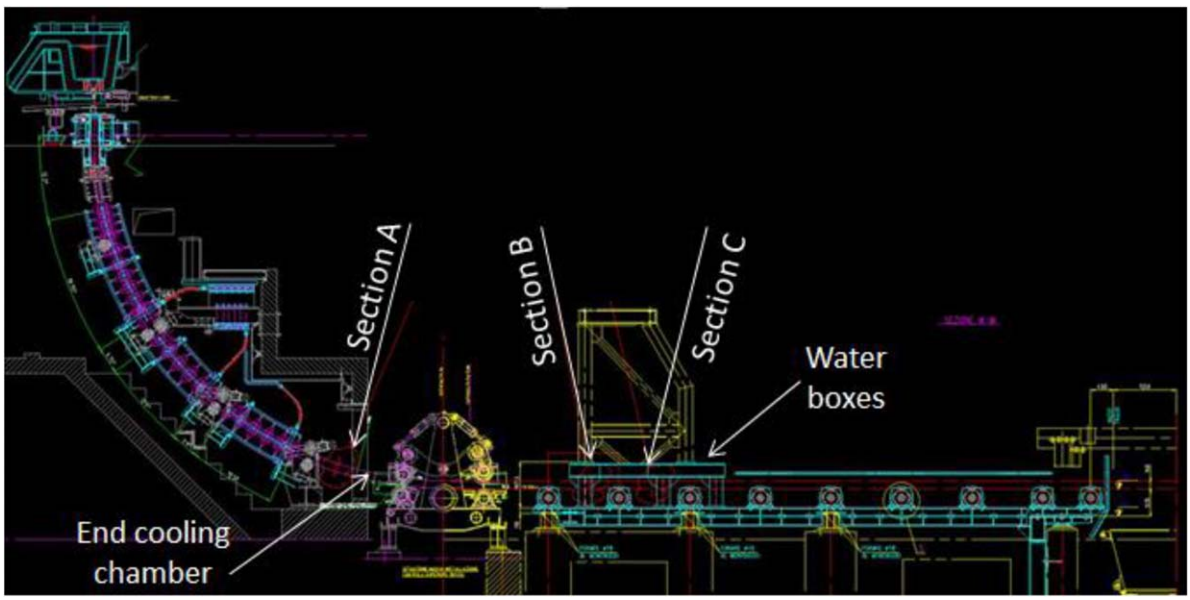

Figure 4. FENO continuous casting machine layout: section A (10 m), section B (14 m) and section C (15.5 m).

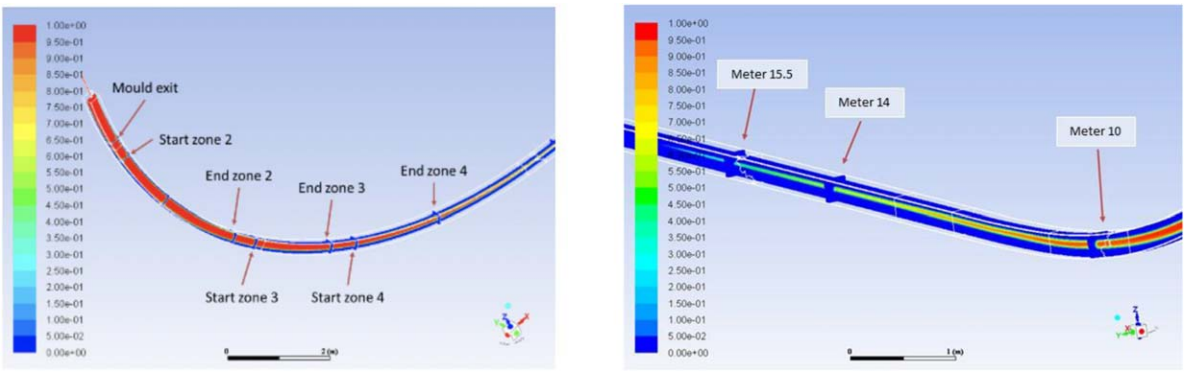

Figure 5. Liquid fraction evolution along the cooling zones (a) and after the secondary cooling chamber (b).

system test the casting speed used was different from those simulated with CFD, between 2.2 and 2.8 m min^{-1}. Since CFD simulations require long computation times, it was decided to simulate the FENO industrial continuous casting process with a TECNALIA's in-house CC thermal model that requires very short computation times, supports transient conditions and was also validated with temperature measurements and compared with CFD simulations.

3.1. Continuous casting machine layout

The FENO continuous casting machine is a six strands machine for 160 × 160 mm billets, with four zones of secondary cooling and some water-cooled panels after the withdrawal unit. Figure 4 shows the layout of the machine, indicating the positions that were initially defined for the installation of the MIT device: section A, at the end of the secondary cooling chamber, and section B and section C within the water boxes.

3.2. CFD modelling

A 3D CFD model for a 160 × 160 mm billet was implemented using ANSYS Fluent code. The model covers from the tundish pouring exit to the cutting shear, with a total strand length of 25 m from the meniscus level. In order to impose the heat extraction in the different cooling zones along the strand length, the following boundary conditions were used.

- *Primary cooling (mold heat extraction)*: a UDF (user defined function) was programed to impose the local heat flux varying along the length of the mold according to equation (10), which was adjusted with bibliography information:

$$\mathrm{q(z)} = \frac{\alpha \rho_w \mathrm{C}_w Q \Delta T_w^T}{\mathrm{P}_m} * \frac{e^{-\alpha z}}{1 - e^{-\alpha \mathrm{H}_{me}}} \tag{10}$$

where α is an experimental constant (1 m^{-1}), ρ_w is density of water (kg m^{-3}), C_w is specific heat of water (j kg^{-1} k^{-1}), Q is volume flow rate of cooling water (m^3 s^{-1}), P_m is perimeter of the tube mold (mm), $h_{spray} = \frac{1570 \times Q_w^{0.55}[1-0.0075 \times T_{water}]}{\beta}$ is distance from meniscus (m) and H_{me} is mold length in contact with the steel (m).

- *Secondary cooling*: a mixed boundary condition of radiation with the ambient conditions of the cooling chamber and forced convention from nozzles was applied. The secondary cooling has four zones: foot roll, zone 2, zone 3 and zone 4. The HTC (heat transfer coefficient) for each zone was calculated using Nozaki's law:

$$\mathrm{h_{spray}} = \frac{1570 \times Q_w^{0.55}[1 - 0.0075 \times \mathrm{T_{water}}]}{\beta} \tag{11}$$

where Q_w is water flux in the spray zone (l m^{-2} s^{-1}), T_{water} is temperature of water (°C) and β is a machine coefficient.

For the adjustment of the machine coefficient, several measurements of the billet surface temperature were done with a thermographic camera (before and after the withdrawal unit) for a Fe50 steel grade with the same casting parameters as those used in the CFD simulations.

- *Zones exposed to air and to water panels*: a mixed boundary condition of radiation and natural convention with the ambient temperature was applied. The heat transfer coefficient and ambient temperature is different at each zone depending on its location along the strand.

Figure 5 shows a general view of the evolution of the liquid fraction in the symmetry and transversal plane at different positions along the strand, from the mold exit to the water boxes location, obtained for the CFD simulation of the steel grade Fe50 and the casting speed 2.65 m min^{-1}.

Figure 6 shows the contours of the liquid fraction of a cross slice of the billet at different positions of the strand length, starting from the mold exit and ending at the water boxes position. The top of each image corresponds to the internal radius face (top face) and the bottom to the external radius face (bottom face) of the billet.

The CFD simulation results were validated with temperature measurements of the billet before and after the withdrawal unit with a thermographic camera and with a

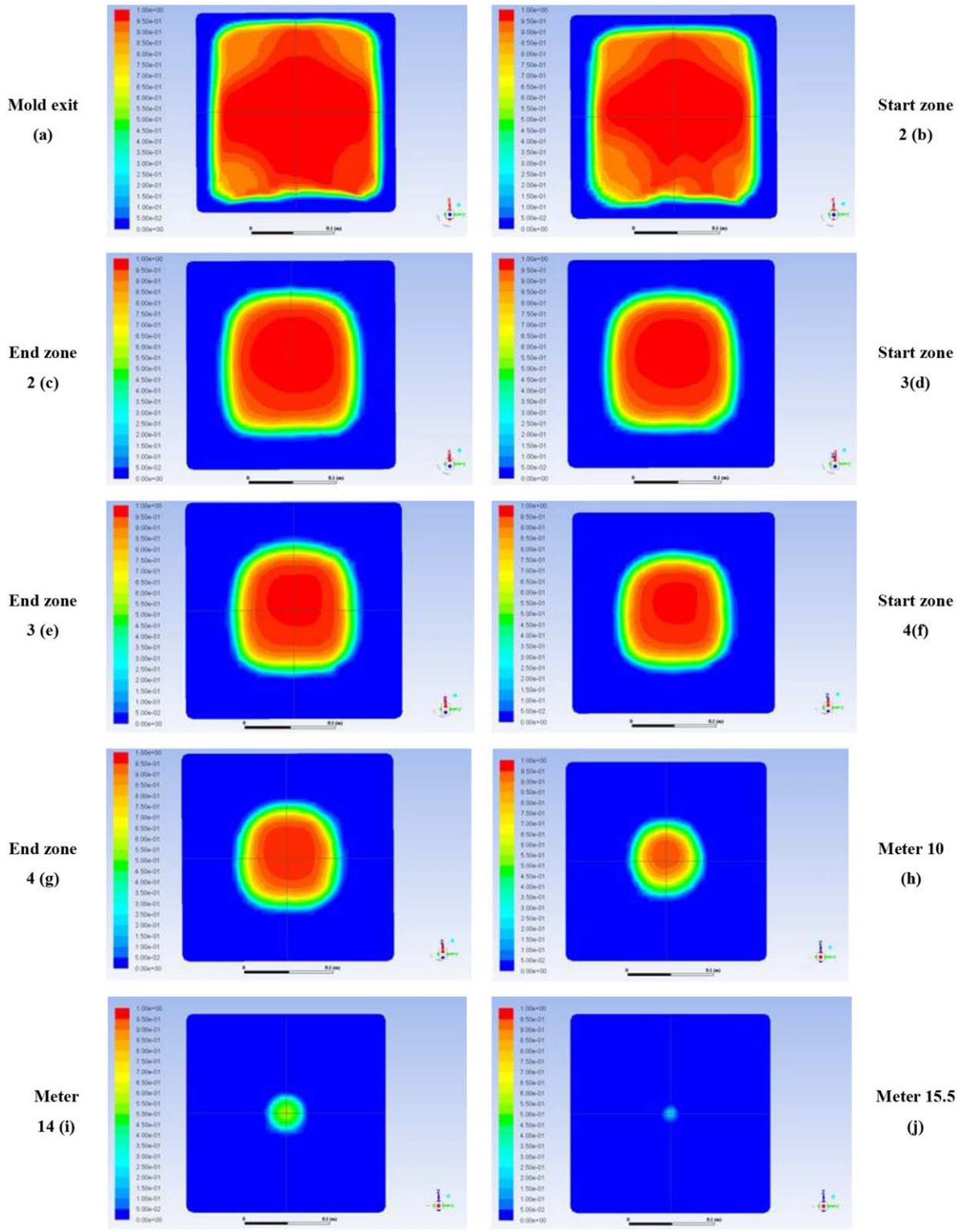

Figure 6. Liquid fraction contours of a cross slice of the billet at various positions of the strand.

macro-etch of a slice under the simulated conditions. The temperatures obtained with the CFD simulation at the same location as the plant measurements were within the range of measured values. In addition, a good correspondence was observed between the location of the final segregation from macro-etch with the final solidification point calculated in the CFD simulation.

3.3. Thermal simulation supporting transient conditions

The continuous casting thermal model developed by TECNALIA predicts the temperature distribution, the shell thickness and the metallurgical length during the solidification process of a billet in a continuous casting machine. The model solves a transient 2D case. Several cross sections of the billet,

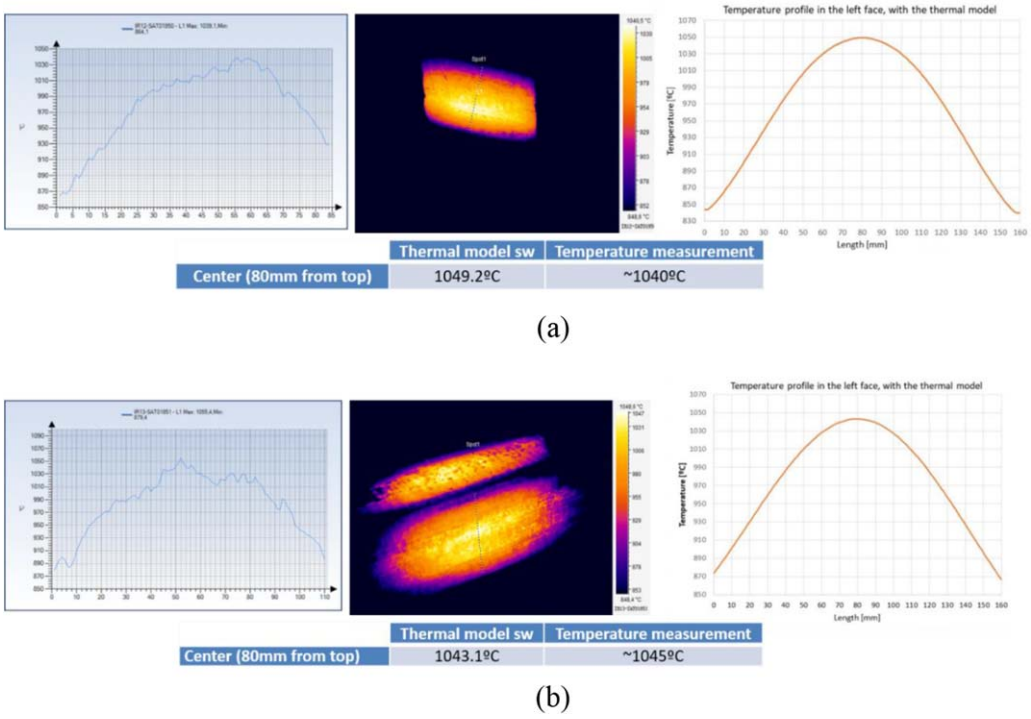

Figure 7. Temperature measurements on one side of the billet before (a) and after (b) the withdrawal unit in comparison with the thermal profile obtained by the thermal model for the same place on the billet.

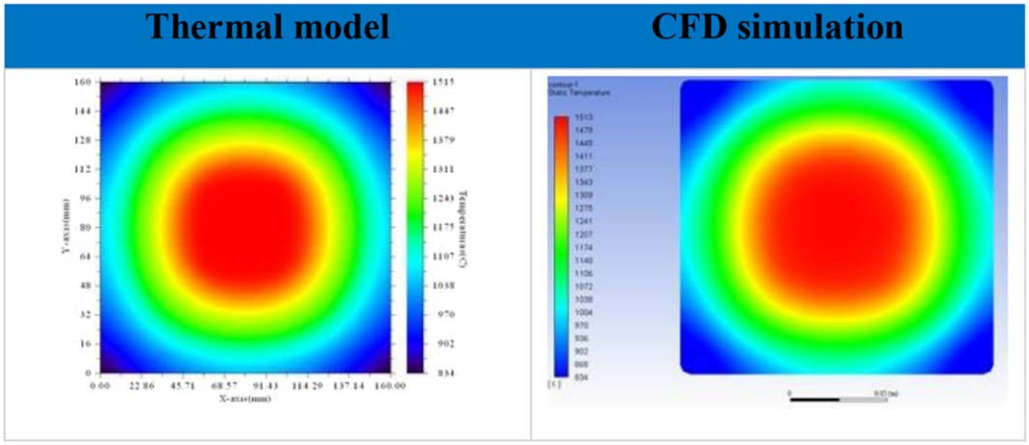

Figure 8. Comparison of the temperature contours obtained with the CFD simulations and the thermal model (Fe50 steel grade and 2.65 m min^{-1} casting speed) in the position where the MIT device was tested (end of the secondary cooling chamber).

distributed along the strand, move through the continuous caster. The model considers the heat exchange with the mold wall and afterwards with the secondary cooling system, rolls and ambient environment. The differential equation that governs the heat transfer and is solved by the model is expressed as

$$\frac{\partial^2 T}{\partial x^2} + \frac{\partial^2 T}{\partial y^2} + \frac{Q}{k(T)} = \frac{\rho(T) \cdot Cp(T)}{k(T)} \frac{\partial T}{\partial t} \qquad (12)$$

where ρ, Cp and k are the density, specific heat and thermal conductivity of the steel grade depending on the temperature, T is the temperature and Q is the transferred heat from the exterior. The thermophysical properties of the steel grade, such as conductivity, specific heat, latent heat, density, and liquidus and solidus temperature are calculated by a commercial software, and depend on steel composition.

The model can solve steady state and transient conditions. In the steady state mode, the process parameters, such as the casting temperature/speed and primary/secondary cooling flow rates, are considered to be constant throughout the simulation. In the transient mode, these values can change in each iteration with the actual process parameters.

The configuration of the FENO continuous casting machine (mould geometry, configuration of the secondary cooling (nozzles type and distribution, rolls, etc), unbending rolls, supporting rolls and water boxes after

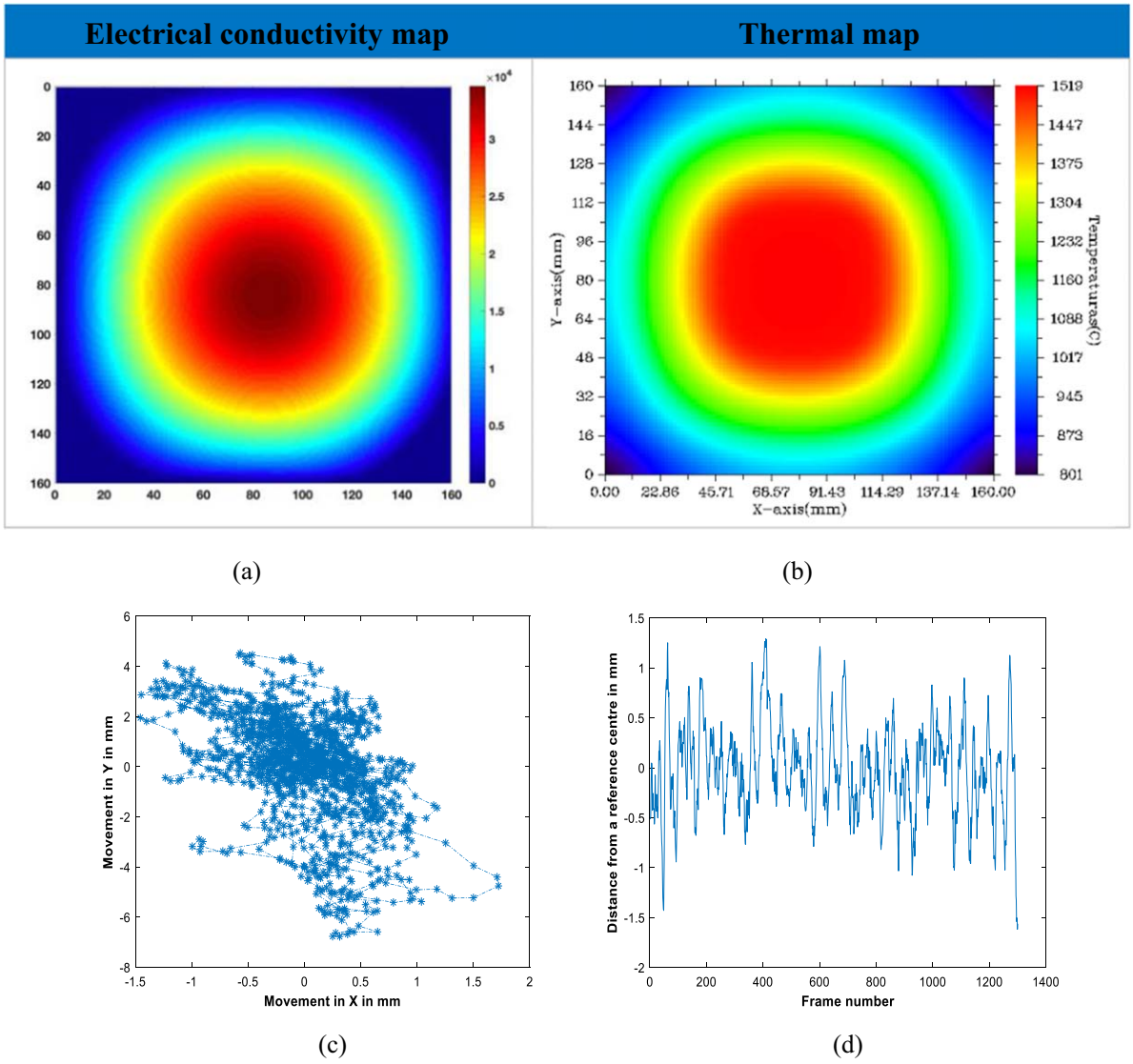

Figure 9. (a) 2D electrical conductivity map and (b) thermal maps of the cross section of the billet at the tomography device position for the analyzed frame (frame 150 654 corresponding to the minute 3332 of the test), (c) movement of billet in x and y in mm for 1300 frames, (d) distance from central point in 1300 frames.

the straightener) was implemented in the model and then validated.

Firstly, the model was validated with temperature measurements. The temperatures on one side of the billet, before and after the withdrawal unit, were measured with a thermographic camera during heating of the Fe50 steel grade. The actual process parameters of the heat were used as input for the thermal model in order to simulate the solidification process of the heat. Figure 7 shows images and graphs of the temperature values, before and after the withdrawal unit, along a line across the measured face, and the thermal profile obtained by the thermal model along the vertical line of the billet face where the temperature was measured. As can be seen, the results of the thermal model are in accordance with the experimental data (less than 10 °C difference in the central point of the face).

Finally, the CFD simulations for the Fe50 steel grade and the casting speeds of 2.65 and 3 m min^{-1} explained above were compared with the results of the thermal model using the same casting parameters as those used in the CFD simulations. Figure 8 shows the temperature contours of the billet section obtained from the CFD simulation and the thermal model at the position where the tomography device was finally installed and tested. As can be seen, the solidification front obtained in both cases is quite similar.

From the results obtained with the thermal model for the external surface of the billet (simulated temperatures in line with the measured temperatures) and for the interior of the billet (solidification fronts similar to those obtained with the CFD simulations), the authors consider that this thermal model is a valid alternative for obtaining the thermal maps of the FENO continuous casting process corresponding to the heating carried out during the MIT device field test, and thus facilitates the analysis and validation of the electrical conductivity maps.

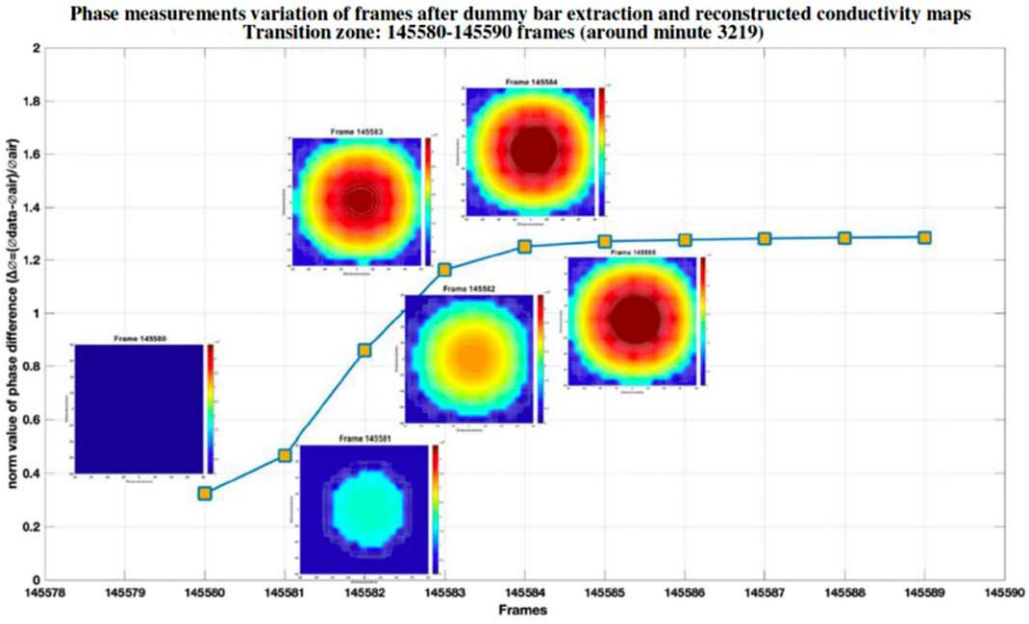

(a)

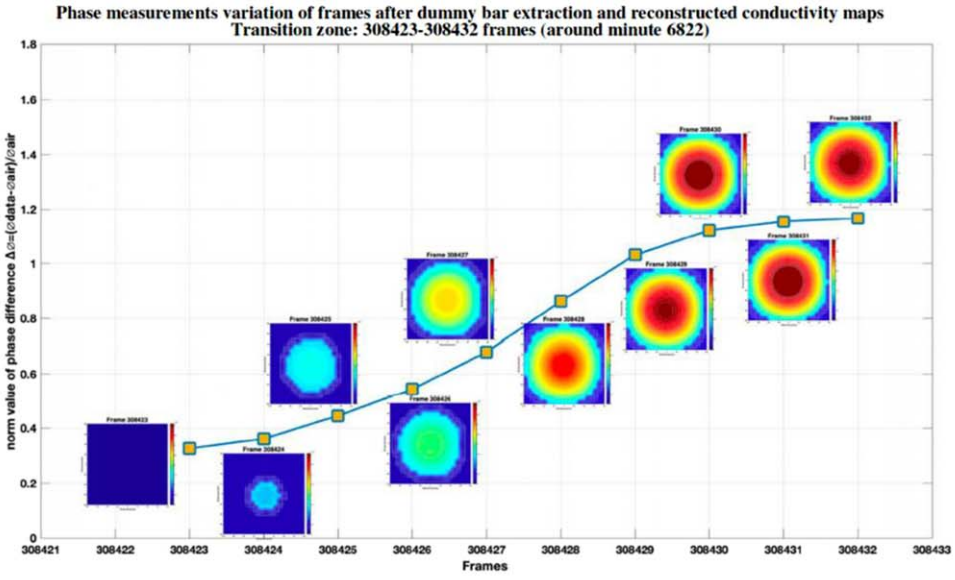

(b)

Figure 10. The reconstructed electrical conductivity maps of some frames after the dummy bar extraction for two Fe50 steel grade casting sequences start. The blue line represents the normalized values of phase difference measured by the tomography device.

4. Results and analysis

4.1. Reconstructed images of the solidification front

As mentioned before, the anisotropic TV algorithm is employed to reconstruct the 2D electrical conductivity maps from the data measured by the tomography device installed in the secondary cooling chamber.

Figures 9(a) and (b) shows the reconstructed electrical conductivity map and the thermal map obtained with the TECNALIA thermal model, using the actual process parameters, for a selected test time. As can be observed, the internal contours (solidification front) obtained by the MIT have the same shape as those obtained by the thermal model: a circular shape. It is possible to compare and calibrate the thermal model with MIT images, although in the absence of a gold standard measurement for interior thermal measurements it is fair that we leave the analysis of the accuracy for future studies. The thermal models are an image of the temperature profile with no movement. In reality, the billet can move, so to enable the comparison of the MIT images with

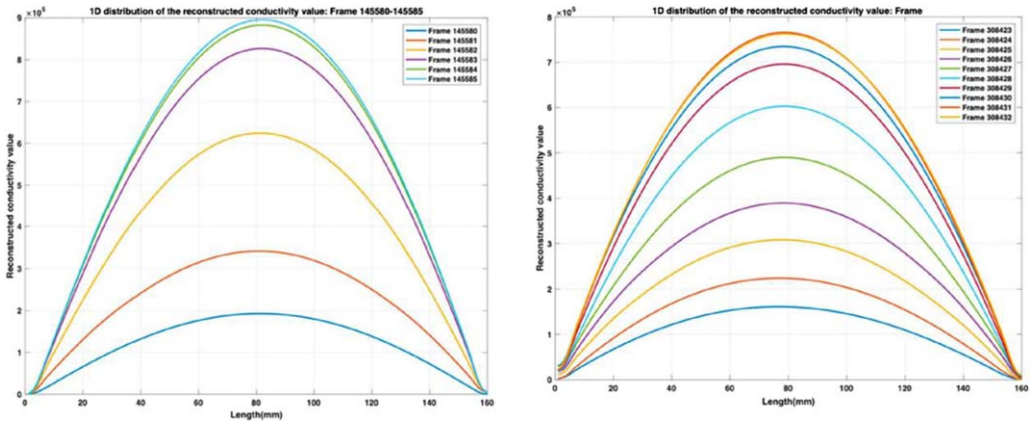

Figure 11. 1D normalized distribution of the reconstructed electrical conductivity values at the center lines for the frames analyzed.

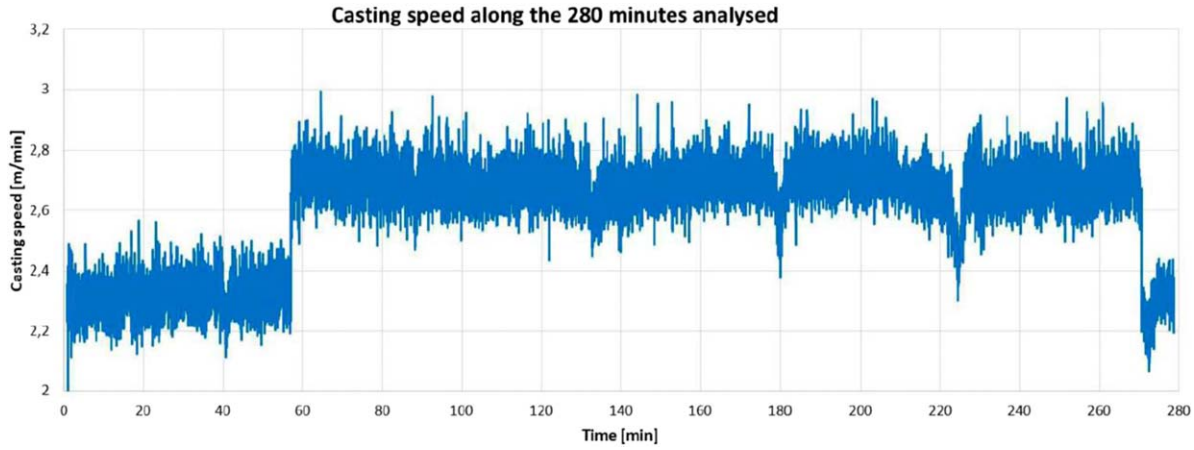

Figure 12. Evolution of the casting speed during the time period selected for the MIT device test.

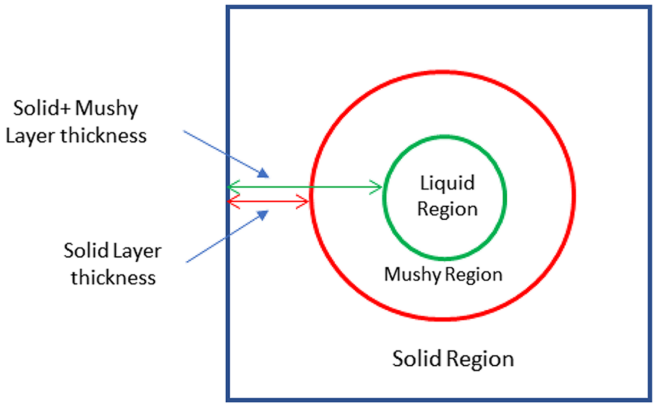

Figure 13. Demonstration of thickness of solid layer and solid + mushy layer.

the thermal model we need to account for positional movement of the billet. This can be done using MIT images and the method proposed in [15]. Figures 9(c) and (d) show the relative movement between the MIT coil array and the billet (mainly due to the billet's mechanical movement). Although the movement could be measured by an additional device, the MIT device can reliably provide a good account of the billet movement that is considered when comparing a thermal model with the MIT images. This shows a movement of a few mm for the billet, mostly vertically.

4.2. Conductivity maps after the dummy bar extraction

At the beginning of a new casting sequence, the dummy bar is extracted together with the head of the billet that is totally solidified. Therefore, the analysis of the evolution of the measurements after the dummy bar extraction allows the analysis of the evolution of the measurements in the transition from a fully solidified section to a solid-mushy one.

Figure 10 displays the reconstructed electrical conductivity maps for nine frames after the dummy bar extraction in two Fe50 steel grade casting sequences start (about minutes 3219 and 6822). With the scanning capacity of the device, a frame corresponds to about 1.3 s. Besides, figure 11 shows the 1D normalized distribution of the reconstructed electrical conductivity values at the centre lines for the selected frames of conductivity maps. Movement of the peak (a shift to the right or left) on these 1D figures correspond to the billet movement such as the ones shown in figures 9(c) and (d). The images in both figures show the evolution of the conductivity values that can be seen in the MIT images The changes in conductivity

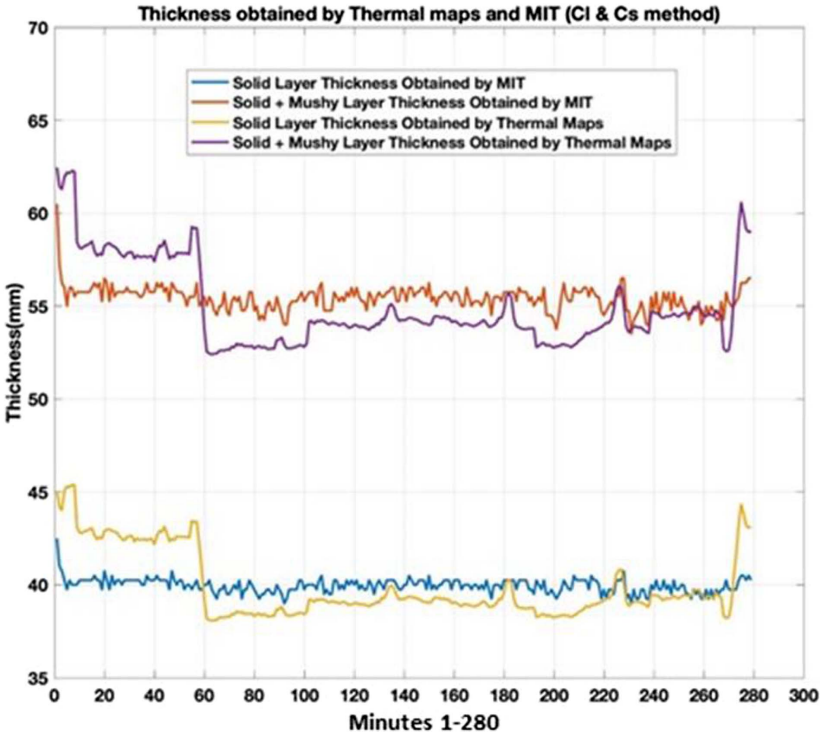

Figure 14. Evolution of the thickness of the solid layer and solid + mushy layer obtained by MIT (using the C_s & C_l values) in comparison with the thickness obtained from the thermal maps, throughout 280 min of casting of Fe50 steel grade.

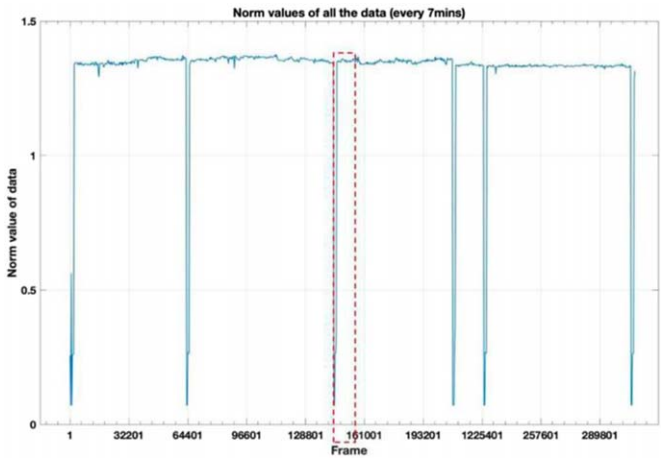

Figure 15. Evolution of the normalized values of phase difference measured by the tomography device during the whole test.

during the extraction of the dummy bar can be high compared to normal operation. It starts with almost constant values for conductivity in the entire billet section, when the temperature is low and there is only a solid phase, and later, when the temperature of the billet increases and therefore the mushy phase appears, the electrical conductivity values in the middle of the section increase. Subsequently, this reaches normal operation in the continuous movement of the hot billet.

The two sets of results prove clearly that the measurements are consistent, and the system can detect the transition from a fully solidified section to a solid-mushy section.

4.3. Conductivity maps along the process

A 280 min period of the field test of the MIT device for a Fe50 steel grade casting was analysed to study the evolution of the shell thickness along the process. Figure 12 shows the evolution of the casting speed in the selected time period, that ranges from 2.2 to 2.8 m min^{-1}.

With the reconstructed data acquired during the test, it was not easy to detect marked changes in the conductivity values along the billet section. Therefore, it was not convenient to obtain a sharp distinction between the different solid–mushy–liquid boundaries. Therefore, in order to calculate the thickness of the solid layer and the thickness of the solid and mushy layer (see figure 13) from a reconstructed electrical conductivity map, we used a mapping function for the thermal distribution and electrical conductivity map obtained for a reference frame. This allowed us to obtain the electrical conductivity values corresponding to the solidus semperature (C_s) and the liquidus lemperature (C_l) of the target steel grade. Then, these values were used to calculate the shell thicknesses in the rest of the frames. In this test, the reference frame was selected within a stable period in the process parameters, obtaining the following values: $C_s = 25\,745$ s m^{-1} and $C_l = 31\,011$ s m^{-1}.

Once the C_s and C_l values were obtained, the process to calculate the shell thicknesses in any frame was as follows: (1) obtain the electrical conductivity map in the frame; (2) obtain the minimum distances from the left/right/top/bottom side to the contour corresponding to the C_s value on the conductivity map; (3) the thickness of the solid layer will be the average of the above four values; (4) obtain the thickness of the solid and

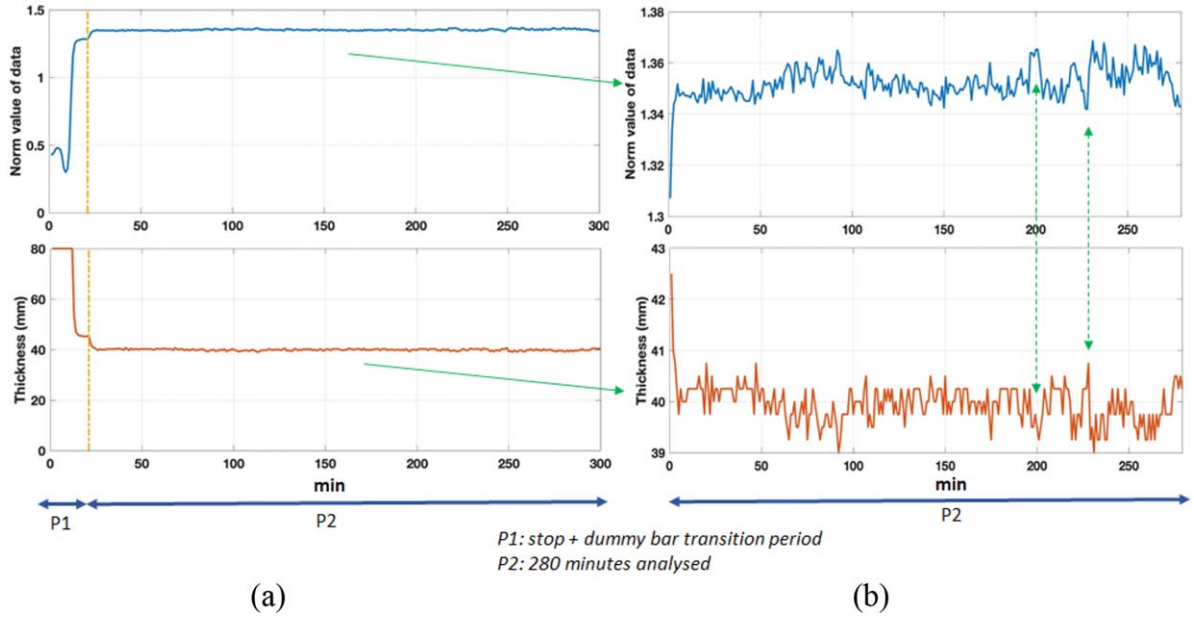

Figure 16. Evolution of the normalized value of phase difference measured by the tomography device during 300 min of a Fe50 steel grade heat including the casting start and evolution of the shell thickness obtained by MIT (a) for entire P1 and P2, and (b) for P2.

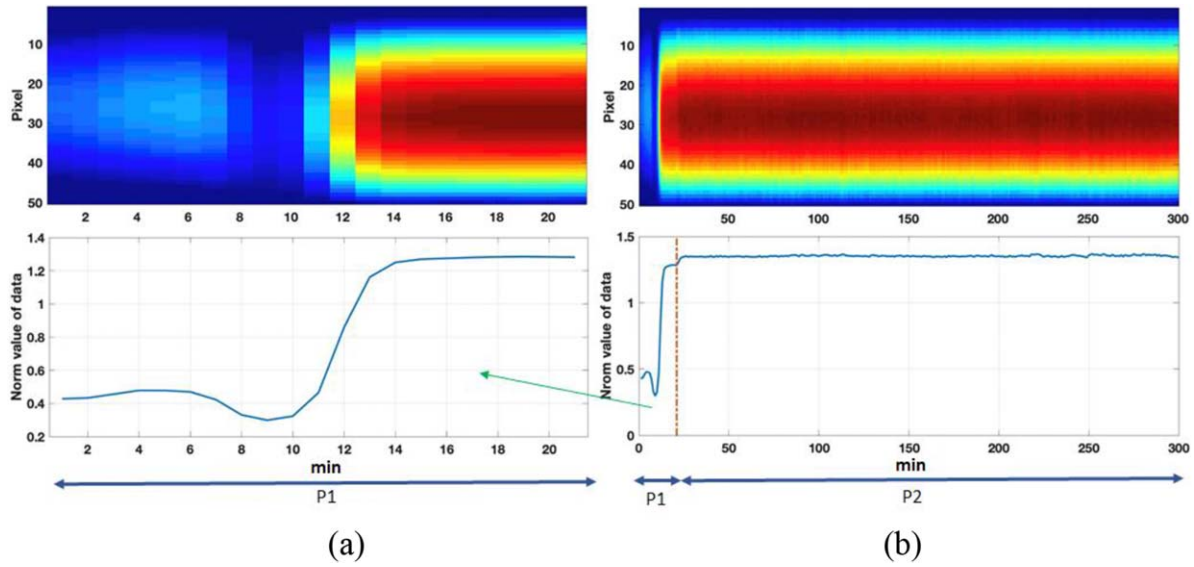

Figure 17. A 2D plot of the middle of the billet along the time analyzed showing as reference the normalized value of phase difference measured by the MIT device (a) for P1, and (b) both P1 and P2.

mushy layer in the same way but using the C_l value. The same method was used to calculate the thicknesses with the thermal maps but using the values of C_s and C_l.

For each minute analyzed, figure 14 displays the thicknesses of the solid layer and solid and mushy layer obtained with the MIT system and the thermal maps, calculated with the TECNALIA thermal model with the actual process parameters recorded during the test.

As can be observed in the figure, the evolution of the thicknesses obtained with the thermal maps is in line with the evolution of the casting speeds (see figure 12). During the first 60 min, with low casting speed, the average thickness of the solid layer is about 42.7 mm and then, when the casting speed increases, the average thickness decreases to about 39 mm. Similarly, for the thickness of the solid + mushy layer, during the first 60 min the average thickness obtained is about 58 mm (i.e. an average radius of liquid area of 22 mm) and then decreases to about 53.9 mm (average radius of liquid area of 26.1 mm). In general, for the process parameters used during the test, the variation in the thickness of the solid layer obtained with the thermal maps is in a narrow range of 5 mm, and the variation in the thickness of the solid and mushy layer, slightly greater, in a range of 6.5 mm.

With respect to the values obtained with the MIT system, as shown in the figure, the values of the thickness of the solid layer obtained are quite stable along the whole period, the average thickness is about 40 mm with a variation range of about 2.5 mm. For the solid and mushy layer, the average

thickness is about 55.5 mm. According to the results, it seems that the changes in the casting speed are not reflected in the shell thicknesses obtained with the MIT system, although it is important to take into account that there were not large changes in the casting speed during the test, they were in the range [2.2–2.8] m min^{-1}, and therefore there were not large changes in the internal structure of the billet.

Figure 15 shows the normalised values of the phase difference measured by the tomography device during the test, calculated every 7 min. It can be observed that the values are quite stable with a very narrow range of variation, except in the case of several large peaks where the value decreases to almost cero, corresponding to sequence changes, and which are followed by a rapid increase after the dummy bar extraction due to the transition from solid to solid-mushy state, as was seen previously (see figure 10). The dashed square highlights the time period that is analysed in more detail in the next figures.

The selected time period includes the 280 min where the shell thickness evolution has been analysed above and some previous time corresponding to the sequence change, 300 min in total. Figure 16 shows the results measured by the MIT device for the evolution of the normalised value of phase difference and the shell thickness of the solid layer with the C_s and C_l values method respectively. It can be observed from the figure that the solid thickness obtained by MIT follows the trend of the data captured by the device.

Besides, figure 17 displays a 2D plot of the middle of the billet along the analysed time, which indicates a legible link between the data captured by the device and the reconstructed conductivity maps.

From both figures a clear correlation can be observed between the data captured by the device, the reconstructed conductivity maps and the shell thicknesses obtained by MIT. So, when there is a large change in the data, for example during the dummy bar extraction and the transition from solid to solid–mushy state, there is also a large change in the shell thicknesses. And when there are almost no changes in the data, for example during the 280 min analysed, no relevant changes in the shell thicknesses are observed either.

5. Conclusion

The MIT device was successfully installed at the end of the secondary cooling chamber of a continuous casting machine. The test showed that the temperature of the copper coils of the device was stable and therefore that the designed cooling system is suitable to work in the harsh operating conditions. In addition, the results obtained with the new MIT system and proposed anisotropic TV inverse algorithm show the capability of the system to monitor the solidification process deep inside the billet. These are the first results of their kind, as far as the authors are aware.

With the real plant data acquired, it is possible to reconstruct the shape of the solidification front and analyse its evolution (increase/decrease) over time. Analysing the accuracy of the MIT data is a challenge since there are no other devices that can do the same measurement. CFD and thermal models can be an alternative to evaluate the consistency of data. Extensive CFD models and a full appreciation of all control parameters in the whole continuous casting process is needed to evaluate the accuracy of the MIT system with higher resolution. But for now, this is a very promising result for the birth of a new tool for continuous casting. The billet movement can be derived accurately using MIT images, allowing a more robust comparison between MIT images and thermal map images.

The evolution of the shell thickness along a casting of the Fe50 steel grade was also analysed. We clearly observed that with the proposed MIT tool it is possible to detect changes in the internal structure of the billet. The more extensive changes, for example during the extraction of the dummy bar, show that the system can detect the change in electrical conductivity and hence the solidification process. In order to detect changes of a few millimetres in a billet of size 160 mm × 160 mm, further optimisation of the system may be needed. Some of the potential improvements identified to achieve a higher sensitivity and resolution of the system are: (i) to reduce the frequency of the device, in order to increase the penetration depth, and (ii) to enlarge the coils, reducing their number, in order to improve the signal-to-noise ratio. But for now this is a very promising result for the birth of a new tool for continuous casting.

Acknowledgement

The SHELL-THICK project has received funding from EU Research Fund for Coal and Steel under Grant No. 709830. This study reflects only the author's views and the European Commission is not responsible for any use that may be made of the information contained therein.

ORCID iD

Manuchehr Soleimani https://orcid.org/0000-0002-6341-9592

References

[1] Limodin N, Salvo L, Boller E, Suéry M, Felberbaum M, Gaillièguе S and Madi K 2009 In situ and real-time 3-D microtomography investigation of dendritic solidification in an Al–10 wt.% Cu alloy *Acta Mater.* **57** 2300–10

[2] Alizadeh M, Jahromi A J and Abouali O 2008 New analytical model for local heat flux density in the mold in continuous casting of steel *Comput. Mater. Sci.* **44** 807–12

[3] Liotti E, Lui A, Kumar S, Guo Z, Bi C, Connolley T and Grant P S 2016 The spatial and temporal distribution of dendrite fragmentation in solidifying Al-Cu alloys under different conditions *Acta Mater.* **121** 384–95

[4] Paradies C, Smith R and Glicksman M 1997 The influence of convection during solidification on fragmentation of the mushy zone of a model alloy *Metall. Mater. Trans.* A **28** 875–83

[5] Wang M, Williams J, Jiang L, De Carlo F, Jing T and Chawla N 2011 Dendritic morphology of α-Mg during the solidification of Mg-based alloys: 3D experimental characterization by x-ray synchrotron tomography and phase-field simulations *Scr. Mater.* **65** 855–8

[6] Lee T L, Khong J C, Fezzaa K and Mi J W 2013 Ultrafast X-ray imaging and modelling of ultrasonic cavitations in liquid metal *Mater. Sci. Forum* **765** 190–4
[7] Maire E and Withers P J 2014 Quantitative X-ray tomography *Int. Mater. Rev.* **59** 1–43
[8] Alizadeh M, Jahromi A J and Abouali O 2008 A new semi-analytical model for prediction of the strand surface temperature in the continuous casting of steel in the mold region *ISIJ Int.* **48** 161–9
[9] Hardin R A, Liu K, Beckermann C and Kapoor A 2003 A transient simulation and dynamic spray cooling control model for continuous steel casting *Metall. Mater. Trans.* B **34** 297–306
[10] Ma L, Spagnul S and Soleimani M 2017 Metal solidification imaging process by magnetic induction tomography *Sci. Rep.* **7** 14502
[11] Soleimani M, Lionheart W R and Peyton A J 2007 Image reconstruction for high-contrast conductivity imaging in mutual induction tomography for industrial applications *IEEE Trans. Instrum. Meas.* **56** 2024–32
[12] Bíró O 1999 Edge element formulations of eddy current problems *Comput. Methods Appl. Mech. Eng.* **169** 391–405
[13] Riviere B 2008 *Discontinuous Galerkin Methods for Solving Elliptic and Parabolic Equations: Theory and Implementation* (Philadelphia, PA: SIAM)
[14] Li F, Abascal J F, Desco M and Soleimani M 2016 Total variation regularization with split Bregman-based method in magnetic induction tomography using experimental data *IEEE Sens. J.* **17** 976–85
[15] Li F, Spagnul S, Odedo V and Soleimani M 2019 Monitoring surface defects deformations and displacements in hot steel using magnetic induction tomography *Sensors* **19** 3005